Chinese Chemical Letters 35 (2024) 108356

Contents lists available at ScienceDirect

Chinese Chemical Letters

journal homepage: www.elsevier.com/locate/cclet

Tuning the exciton binding energy of covalent organic frameworks for efficient photocatalysis

Zhangjie Gu[a], Zhen Shan[a], Yulan Wang[b], Jinjian Wang[a], Tongtong Liu[a], Xiaoming Li[c], Zhiyang Yu[b], Jian Su[a,*], Gen Zhang[a,d,*]

[a] Key Laboratory for Soft Chemistry and Functional Materials of Ministry of Education, School of Chemistry and Chemical Engineering, Nanjing University of Science and Technology, Nanjing 210094, China
[b] State Key Laboratory of Photocatalysis on Energy and Environment, College of Chemistry, Fuzhou University, Fuzhou 350002, China
[c] MIIT Key Laboratory of Advanced Display Material and Devices, School of Materials Science and Engineering, Nanjing University of Science and Technology, Nanjing 210094, China
[d] Key Laboratory of Preclinical Study for New Drugs of Gansu Province, School of Basic Medical Sciences, Lanzhou University, Lanzhou 730000, China

ARTICLE INFO

Article history:
Received 31 January 2023
Revised 19 February 2023
Accepted 20 March 2023
Available online 22 March 2023

Keywords:
Covalent organic frameworks
Exciton binding energy
Atom substitution
Extended conjugation
Photocatalysis

ABSTRACT

Owing to the large exciton binding energy (>100 meV) of most organic materials, the process of exciton dissociation into free electrons and holes is seriously hindered, which plays a key role in the photocatalytic system. In this study, a series of chalcogen (S, Se)-substituted mesoporous covalent organic frameworks (COFs) have been synthesized for enhanced photocatalytic organic transformations. Photoelectrochemical measurements indicate that the introduction of semi-metallic Se atom and the enlargement of conjugation degree can not only reduce the exciton binding energy accelerating the charge separation, but also reduce the band gap of COFs. As a result, the COF-NUST-36 with the lowest exciton binding energy (39.5 meV) shows the highest photocatalytic performance for selective oxidation of amines (up to 98% Conv. and 97.5% Sel.). This work provides a feasible method for designing COFs with high photocatalytic activity by adjusting exciton binding energy.

Solar energy is the main source of many energies on the earth, featuring the advantage of clean and renewable. Converting solar energy into chemical energy in the form of higher-value chemicals has aroused intensive interest [1–4]. The key to successful implementation of this process lies in the use of light and rationally design of photocatalysts [5–7]. During the past decades, various advanced photocatalysts, such as TiO_2, $BiVO_4$, g-C_3N_4 and COFs [8,9] have been designed and prepared. Among them, the limited structural designability and narrow visible light absorption range of TiO_2, $BiVO_4$ and g-C_3N_4 impede their further applications. COFs are a completely designed crystalline material with low density, excellent stability, functional diversity, and tunable electric structures [10–14]. With these features, COFs have emerged as a promising platform for potential applications in photocatalytic hydrogen evolution [15–17], carbon dioxide reduction [18,19], degradation of pollutants [20,21] and organic transformations [22–26]. Unfortunately, owing to the partial crystallinity, inefficient charge separation and limited electron transport capability, the photocatalytic performance of COFs is undesirable. In particular, the charge separation is a crucial factor in photocatalytic process. However, the generation and separation efficiency of charge carriers is directly related to exciton binding energy (E_b) in strong exciton system [27]. The Coulomb interactions that stabilize the exciton with regard to electrons and holes referred to as the E_b [28] and the evaluation of E_b is based on an investigation of the quenching of the integrated photoluminescence (PL) intensity with the temperature [29]. In fact, most of the COFs belong to strong exciton system, and they possess a high E_b (typically E_b >100 meV) [30]. It means that the COFs will firstly generate electron-hole pairs bound by Coulomb interactions, namely the Frenkel exciton [28,31], in the process of photocatalysis. The strong Coulomb interactions of the Frenkel exciton will lead to exciton annihilation, seriously hampering the generation of electrons and holes [32–34]. Hence, minimizing the E_b of the COFs to obtain high photocatalytic activity is very attractive but remains a challenge.

To date, many efforts have been dedicated to minimizing the value of E_b in organic photocatalysts [35,36]. Wang and co-authors had realized the reduction of E_b (88 meV) by regulating charge-transfer pathway in linear conjugated polymers [37]. Yin and co-authors had proposed an effective approach to reduce the E_b

---

* Corresponding authors.
E-mail addresses: sujian@njust.edu.cn (J. Su), zhanggen@njust.edu.cn (G. Zhang).

https://doi.org/10.1016/j.cclet.2023.108356

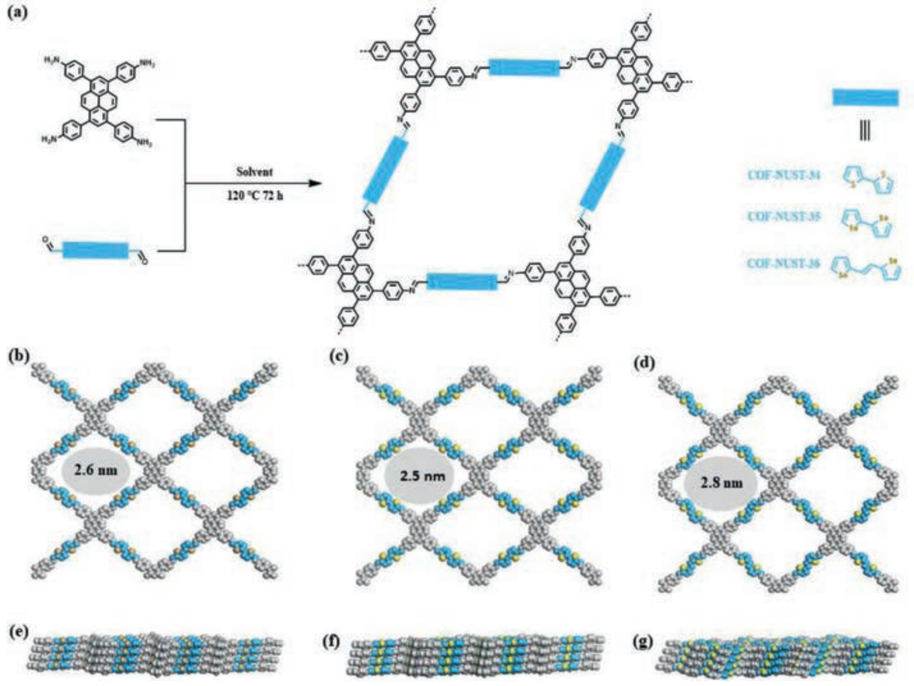

Fig. 1. (a) Synthetic routes of COF-NUST-34, COF-NUST-35 and COF-NUST-36. Top and side views of (b, e) COF-NUST-34, (c, f) COF-NUST-35 and (d, g) COF-NUST-36.

(338 meV) of carbon nitrides (PCN) *via* a method of regulating spin-polarized electrons for photocatalysis hydrogen production [38]. Although these photocatalysts can effectively reduce the value of E_b in amorphous polymers, it is difficult to understand the relationship between tailor-made structure and exciton behaviors. Recently, inspired by the low E_b of solar cells with donor (D)-acceptor (A) structure, Gu and colleagues had built four D-A COFs to minimize the E_b (50.4 ± 1.8 meV) [27]. Unfortunately, the unique structure will lead to rapid reverse charge recombination concurrently [39]. Therefore, it is imperative to propose a new strategy to design photocatalysts with long-range ordering and low E_b.

As a proof-of-concept, we propose a strategy of single atom substitution and increasing conjugation degree to reduce E_b of COFs for the first time. As well known, thiophene and selenophene-based materials have excellent photoelectric properties, which are widely used in organic field-effect transistors [40] and solar cells [41,42]. Compared with thiophene, selenophene has stronger ability of electron supplication. In addition, intermolecular Se···Se interaction is conducive to charge transfer. Herein, three chalcogen (S, Se)-contained mesoporous COFs (COF-NUST) were synthesized starting from a planar conjugated pyrene moity [43]. Photoelectrochemical measurements reveal that the E_b values and band gaps of COF-NUST were gradually decreased with the substitution of S atoms by Se atoms and the conjugation degree increased. Impressively, the COF-NUST-36 shows a quite low E_b (39.5 meV) among reported pristine COFs [27,44,45], which is even close to some inorganic semiconductors, such as MoS_2 [46], GaN [47] and metal-halide perovskites [29,48]. Consequently, the rare example of selenophene-based COF [49], COF-NUST-36 shows effective exciton splitting and the highest photocatalytic activity in the selective oxidation of amines.

The COF-NUST were synthesized by linking TAPP to different building blocks, BTDC, BSDC and EBSDC in the solvothermal condition (Fig. 1). In detail, COF-NUST-34 and COF-NUST-35 were synthesized by the Schiff-base reaction of TAPP and BTDC or BSDC in the presence of 6 mol/L acetic acid using *o*-dichlorobenzene (*o*-DCB) and *n*–butyl alcohol (*n*-BuOH) as solvent at 120 °C for 72 h. COF-NUST-36 was synthesized similar to COF-NUST-34 except that EBSDC, mesitylene and benzyl alcohol were used.

The formation of COF-NUST were evidenced by various analytical methods. Fourier transform infrared (FT-IR) spectra (Figs. S6-S8 in Supporting information) revealed the −C=N− stretching vibrations of COF-NUST-34, COF-NUST-35 and COF-NUST-36 were located at 1610, 1646 and 1648 cm^{-1}, respectively, while the amino stretching vibration peak (~3335 cm^{-1}) and the carbonyl stretching vibration peak (~1688 cm^{-1}) from the building blocks were almost disappeared, indicating the conversion of aldehyde and amino groups. The solid-state ^{13}C NMR spectra (Figs. S9-S11 in Supporting information) also confirmed the formation of −C=N− bond, which at 152, 158, 159 ppm corresponding to COF-NUST-34, COF-NUST-35 and COF-NUST-36, respectively. The element compositions of COF-NUST were confirmed by X-ray photoelectron spectroscopy (XPS). From the total spectra, we can clearly observe the characteristic peaks of C 1s, N 1s and S 2p for COF-NUST-34 (Fig. S12 in Supporting information). For COF-NUST-35 and 36 (Figs. S13 and S14 in Supporting Information), the characteristic peaks of C 1s, N 1s and Se 3d were observed. The N 1s spectra of all COF showed typical peaks, located at 398.8, 399.4 and 399.2 eV, which is ascribed to −C=N− bond in COF-NUST-34, COF-NUST-35 and COF-NUST-36, respectively. All these results manifest the successful synthesis of COF-NUST.

The precise periodical structures of COF-NUST-34, COF-NUST-35, and COF-NUST-36 were verified by powder X-ray diffraction (PXRD) together with structural simulations. The intensive peaks were observed in Figs. 2a-c, indicating the high crystallinity of COF-NUST. The PXRD pattern of COF-NUST-34 exhibited distinguishable peaks at $2\theta = 3.29°$, 4.84°, 6.59°, 9.89°, 13.49°, which are assigned to the (110), (200), (220), (330) and (060) planes. COF-NUST-35 exhibited similar distinguishable peaks at $2\theta = 3.27°$, 4.40°, 4.84°, 6.54°, 9.82°, corresponding to the (110), (200), (020), (220) and (330) planes. The diffraction peaks of COF-NUST-36 at $2\theta = 3.12°$, 4.62°, 6.26°, 9.39° were assigned to the (110), (200), (220) and (330) planes. According to the similar structure reported in the previous literature, the AA and AB stacking crystal mod-

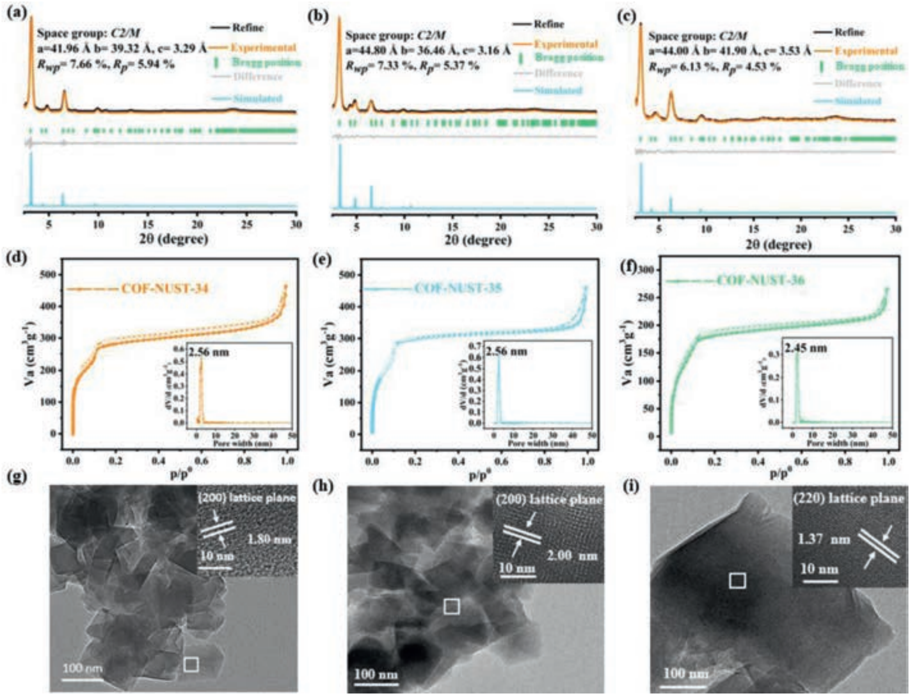

Fig. 2. PXRD patterns of (a) COF-NUST-34, (b) COF-NUST-35 and (c) COF-NUST-36. The N_2 adsorption-desorption isotherms at 77 K and pore size distribution of (d) COF-NUST-34, (e) COF-NUST-35 and (f) COF-NUST-36. High-resolution transmission electron microscopy (HRTEM) of (g) COF-NUST-34, (h) COF-NUST-35 and (i) COF-NUST-36. The Pawley refined pattern in black, experimental profiles are in yellow, simulated pattern for AA stacking in blue, Bragg position in green and difference plot in gray.

els were generated, the experimental diffraction patterns of COF-NUST matched well with AA stacking (Fig. S15 in Supporting information). Pawley refinement was conducted to obtain the unit cell parameters (a = 41.96 Å, b = 39.32 Å, c = 3.29 Å, α = 90°, β = 60.77°, γ = 90°, R_{wp} = 7.66%, R_p = 5.94% for COF-NUST-34; a = 44.80 Å, b = 36.46 Å, c = 3.16 Å, α = 90°, β =63.46°, γ = 90°, R_{wp} = 7.33%, R_p = 5.37% for COF-NUST-35; a = 44.00 Å, b = 41.90 Å, c = 3.53 Å, α = 90°, β = 60.12°, γ = 90°, R_{wp} = 6.13%, R_p = 4.53% for COF-NUST-36).

The porosity of COF-NUST-34, COF-NUST-35 and COF-NUST-36 was assessed by N_2 sorption isotherm at 77 K (Figs. 2d-f). The type IV pattern of COF-NUST indicated that COF-NUST are mesoporous material. The Brunauer–Emmett–Teller surface areas were 1098.7, 1163.1 and 677.7 m²/g for COF-NUST-34, COF-NUST-35 and COF-NUST-36, respectively. Although the skeleton structures of COF-NUST were similar, the crystallinity and framework integrity of COF-NUST-36 obtained by EBSDC were inferior to those of COF-NUST-34 and COF-NUST-35, resulting in a lower specific surface area. Based on the adsorption curve and the nonlocal density functional theory model (NLDFT), the pore-size distribution was calculated to be 2.56, 2.56 and 2.45 nm for COF-NUST-34, COF-NUST-35 and COF-NUST-36, which was identical to the simulated values. Thermogravimetric analysis (TGA) (Fig. S16 in Supporting information) indicated that the three COFs possessed excellent thermal stability and were thermally stable up to 400 °C under N_2 atmosphere. The good chemical stability of COF-NUST-36 was evidenced by the retained PXRD patterns (Fig. S17 in Supporting information) after immersed in tetrahydrofuran, *N,N*-dimethylformamide, 1 mol/L HCl, 1 mol/L NaOH, and visible light irradiation at 25 °C for 24 h. Scanning electron microscopy (SEM) (Figs. S18-S20 in Supporting information) showed that the morphology of COF-NUST-34, COF-NUST-35, and COF-NUST-36 are both lamellar. High-resolution transmission electron microscopy (HRTEM) (Figs. 2g and h) evidenced the excellent crystallinity and indicated the spacing of the lattice fringe (~1.80 nm, ~2.00 nm) corresponded to the lattice planes of (200) for COF-NUST-34, COF-NUST-35, respectively. The spacing of the lattice fringe (~1.37 nm) (Fig. 2i) corresponded to the lattice planes of (220) for COF-NUST-36.

UV–vis diffuse reflectance spectroscopy (Fig. 3a) shows the broad absorption of COF-NUST in the visible region, which originating from the π-conjugated structure of COFs and the building blocks of excellent light absorption capacity (Fig. S21 in Supporting information). Notably, the trend of light absorption in the linkers (absorption region: EBSDC > BSDC > BTDC) is similar in COFs (absorption region: COF-NUST-36 > COF-NUST-35 > COF-NUST-34). By using the Kubelka-Munk function $(\alpha h\nu)^2 = A(h\nu - E_g)$, where α is the absorption coefficient, h is the Planck constant, ν is the frequency and A is the constant, the optical band gaps (E_g) of COF-NUST-34, 35 and 36 were determined to be 1.98, 1.90 and 1.80 eV, respectively (Fig. 3b). Obviously, the E_g of COF-NUST-36 is the narrowest, which is mainly due to the extended conjugation and the semimetal Se atoms with a lower ionization potential [50]. Mott–Schottky (M–S) (Fig. S22 in Supporting information) plot was used to estimate the conduction band value (E_{CB}). The positive slops of MS plots indicated that the COF-NUST are n-type semiconductors. Typically, the E_{CB} is equal to flat band potentials for n-type semiconductors. Accordingly, the E_{CB} of COF-NUST-34, COF-NUST-35 and COF-NUST-36 are estimated to be −1.02, −1.08 and −1.11 V (*vs.* Ag/AgCl), respectively (Fig. 3c). According to the formula $E_{CB} = E_{VB} - E_g$, the valence band values (E_{VB}) of COF-NUST-34, COF-NUST-35, and COF-NUST-36 are 0.96, 0.82 and 0.69 V (*vs.* Ag/AgCl), respectively. Theoretically the lowest occupied molecular orbital (LUMO) and the highest occupied molecular orbital (HOMO) levels of COF-NUST have sufficient potentials to reduce O_2 to superoxide anion $O_2^{\bullet-}$ (E_{red} = −0.48 V *vs.* Ag/AgCl) [51] and oxidize benzylamine into a cation free radical (E_{oxi} = +0.56 V *vs.* Ag/AgCl) [52,53]. Hence, all COF-NUST can be latent photocatalyst for oxidative coupling of amines.

The molecular orbital diagrams of COF-NUST were obtained by density functional theory (DFT) calculation. The charge distributions of HOMO (Fig. 3d) and LUMO (Fig. S23 in Supporting information) in COF-NUST-34 are simultaneously located at BTDC and

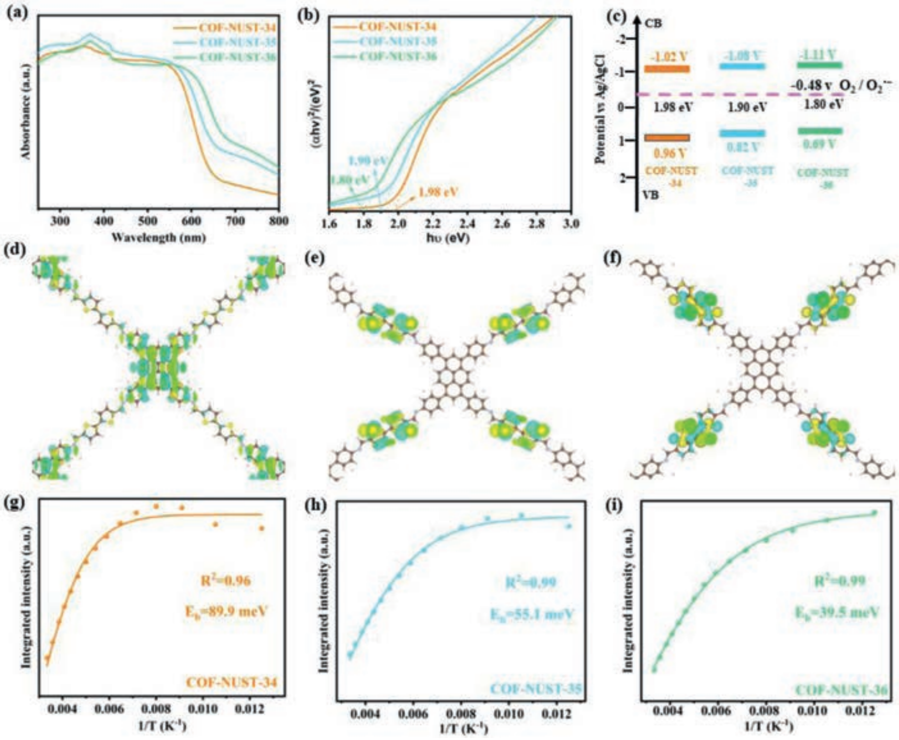

Fig. 3. (a) UV–vis diffuse reflectance spectra of COF-NUST. (b) Tauc plot for estimating the band gap energies of COF-NUST. (c) Band alignment. (d-f) HOMO of COF-NUST-34, COF-NUST-35 and COF-NUST-36. (g-i) Integrated PL emission intensity as a function of temperature of COF-NUST-34, COF-NUST-35 and COF-NUST-36.

TAPP. The high levels overlap of HOMO and LUMO will lead to rapid recombination of charge carriers in COF-NUST-34. The charge distribution of HOMO in COF-NUST-35 (Fig. 3e) is only located at BSDC, while the charge of LUMO (Fig. S24 in Supporting information) is mainly distributed TAPP and BSDC. For COF-NUST-36, the charge distribution of HOMO (Fig. 3f) is only located at EBSDC, while the charge of LUMO (Fig. S25 in Supporting Information) is mainly distributed TAPP and EBSDC. Although partial overlap of HOMO and LUMO, electron-hole pairs can be separated effectively in COF-NUST-35 and 36. These results imply that COF-NUST-35 and 36 may have better photocatalytic performance.

To unveil the charge recombination and separation kinetics of COF-NUST, the temperature-dependent photoluminescence (TD-PL) (Figs. S26-S28 in Supporting information) spectra were measured. The value of E_b was estimated by fitting the integrated PL intensity with the temperature according to Arrhenius equation, $I(T) = I_0/(1 + A\exp(-E_b/k_BT))$ [54]. Accordingly, the E_b values for COF-NUST-34, COF-NUST-35 and COF-NUST-36 were estimated to be 89.9 meV, 55.1 meV and 39.5 meV (Figs. 3g-i), respectively. Notably, the E_b of COF-NUST-36 is significantly lower than COF-NUST-34 and COF-NUST-35, which means that excitons can be more easily dissociated into free carriers. It is worth noting that such low E_b (39.5 meV) is rare observed in COFs [27,44,45] or even inorganic materials such as MoS_2, GaN and metal-halide perovskites (Table S4 in Supporting information) [29,46-48]. Meanwhile, these results indicate that the E_b can be reduced by single atom substitution and enlarging conjugation degree.

Since charge migration is directly related to E_b [55,56], we also systematically studied the charge mobility. As shown in room-temperature PL (Fig. 4a), COF-NUST-36 showed obvious PL quenching compared with COF-NUST-34 and COF-NUST-35, it indicated that the recombination of photogenerated carrier was suppressed. Time-resolved photoluminescence (TRPL) (Figs. S29-S32 in Supporting information) revealed the fluorescence lifetime of COF-NUST-36 (0.57 ns) is the shortest among the three materials (0.80 ns for COF-NUST-34, 0.75 ns for COF-NUST-35), suggesting that electron transport was accelerated in COF-NUST-36.

To further confirm the modulation of charge mobility in COF-NUST, we conducted a series of photoelectrochemical measurements. The transient photocurrent spectra indicated the photocurrent density (Fig. S33 in Supporting information) increases gradually from COF-NUST-34 to COF-NUST-36, implying that the Se atom and extended conjugation are conductive to the separation of charges. Electrochemical impedance spectroscopy (EIS) (Fig. 4b) also proves this result, the semicircular radius of COF-NUST-34 is the largest among three COFs, suggesting that the slowest charge transport [57]. Moreover, Linear sweep voltammetry (LSV) curves showed that the COF-NUST-36 has the highest cathodic photocurrent, whether under visible light illumination (Fig. 4c) or in the dark (Fig. S34 in Supporting information). Thus, we conclude that the lower of E_b can improve charge separation and mobility.

Imines, also known as Schiff bases, are widely used in various organic reactions, pharmaceutical intermediates, and fine chemicals. The traditional synthesis of imines often require acid as catalyst, which inevitably leads to waste of resources and environmental pollution. Photocatalytic selective oxidation provides a convenient and environmentally friendly method for the preparation of imines [58,59]. Accordingly, we used the oxidative coupling of amines to imines under blue light irradiation to evaluate the photocatalytic activity of these COFs. As shown in Table 1, entries 1–3, COF-NUST-36 clearly exhibited the highest conversion (97%) compared with COF-NUST-34 (40%) and COF-NUST-35 (82%) under optimal conditions. It can be accessible to the lowest E_b of COF-NUST-36, the excitons can effectively dissociate into charge carriers. Notably, with a prolonged reaction time (Table 1, entries 4 and 5), the conversion increased, while the selectivity decreased. So, the reaction time must be strictly controlled. We also conducted control experiments (Table 1, entries 6–8) to study the effects of catalyst, visible light irradiation and oxygen atmosphere on photocatalytic efficiency. With the absence of catalyst, the reaction will not take

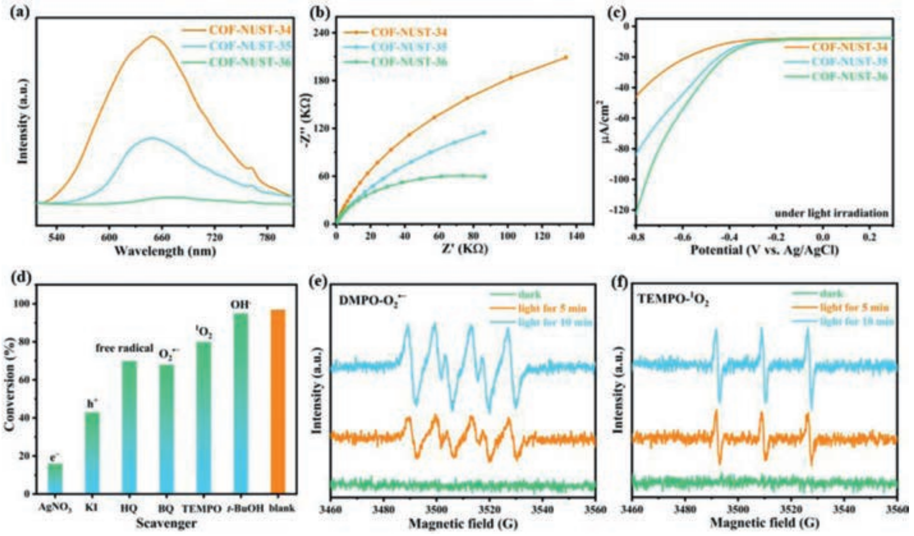

Fig. 4. (a) Room-temperature PL spectra of COF-NUST. (b) EIS spectra of COF-NUST. (c) Linear sweep voltammetry curves of COF-NUST under light irradiation. (d) Effect of scavengers on the photocatalytic oxidation of benzylamine. (e) *In situ* EPR signals labeled by DMPO for $O_2^{\bullet -}$ in dispersions. (f) *In situ* EPR signals labeled by TEMPO for $^1O_2$ in dispersions.

Table 1

Photocatalytic selective aerobic oxidation of benzylamine under blue light[a].

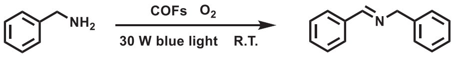

Entry	Photocatalyst	30 W blue light	O_2	Conv. (%)	Sel. (%)
1	COF-NUST-34	+	+	40	99
2	COF-NUST-35	+	+	82	99
3	COF-NUST-36	+	+	97	95
4[b]	COF-NUST-36	+	+	86	99
5[c]	COF-NUST-36	+	+	98	93
6	COF-NUST-36	–	+	4	99
7	No	+	+	<1	n.d.
8	COF-NUST-36	+	N_2	13	99
9	COF-NUST-36	+	air	84	99

[a] Reaction conditions: substate (0.1 mmol), photocatalyst (4.0 mg), O_2 (1 atm), CH_3CN (1.5 mL), 30 W blue light (λ = 455–460 nm), room temperature, 2.5 h. Determined by ^1H NMR. For details, see the experimental section in Supporting information.

[b] 1.5 h.

[c] 3.0 h.

place. Without visible light irradiation or under N_2 atmosphere, only trace product was obtained. Furthermore, air was used instead of oxygen (Table 1, entry 9), the reaction proceeded smoothly with a conversion of 84% realized in 2.5 h, which shows that COF-NUST-36 has high photocatalytic activity.

To explore the general applicability of the COF-NUST-36 photocatalysis for selective aerobic oxidation, benzylamine derivatives bearing different substituents were selected as substrates. All substrates can be transformed into the corresponding imines within 5 h (Scheme 1). In detail, the reaction of benzylamines bearing with electron-donating groups to afford marginally higher conversion and lower reaction time than benzylamines bearing with electron-withdrawing groups. For example, the **2d** ($-OCH_3$) can obtain a conversion of 97% in 2 h, however, the conversion of **2k** is 94% in 4.5 h ($-CF_3$), which is the electron-donating groups can better stabilize the cationic radical intermediate. Besides, the steric hindrance also has an obvious influence on the conversion. Such as piperonylamine (Scheme 1, **2l**) or substituents in the adjacent position (Scheme 1, **2i**) could slow down the reaction processed compared to benzylamine (Scheme 1, **2b**). As a result, transforming into the corresponding imines with slightly prolonged time. Interestingly, The COF-NUST-36 also shows a high conversion (96%) for the oxidative coupling of heterocyclic amine (Scheme 1, **2a**). At last, COF-NUST-36 shows high efficiency and general applicability in oxidation of benzylamine derivatives with difference size. This can be ascribed to the meso–pores in COF-NUST-36.

The good durability of the COF-NUST-36 photocatalyst was confirmed by cycling experiment (Fig. S35 in Supporting Information). The photocatalytic efficiency of COF-NUST-36 can be well remained after being reused for three cycles. The crystallinity of COF-NUST-36 was essentially retained from the PXRD patterns and FTIR spectra after 3 runs, the lamellar morphology was also kept in SEM image.

To investigate the possible mechanism for the oxidative coupling of amines, we chose different scavengers to trap reactive oxygen species (ROS) (Fig. 4d). With the introduction of electron scavenger $AgNO_3$ and hole scavenger KI, the conversion dramatically decreased to 16% and 41%, which indicated that the oxidative coupling of amines is associated with photogenerated electrons and holes. The superoxide radical anions ($O_2^{\bullet -}$) scavenger benzoquinone (BQ) and singlet oxygen ($^1O_2$) scavenger 2,2,6,6-tetramethylpiperidine-1-oxyl (TEMPO) was added to photocatalysis system, a decrease in conversion was observed, illustrating that active species $O_2^{\bullet -}$ and $^1O_2$ both play important roles in the reaction. Moreover, when the radical scavenger hydroquinone (HQ) was added, the conversion dropped to 70%, proved that the oxidation coupling involved a radical process. The addition of *t*-BuOH led to a slight decrease in conversion (95%), which implied that the hydroxyl radical ($^{\bullet}OH$) play a minor role in photocatalytic process.

Electron paramagnetic resonance (EPR) spectroscopy was conducted to confirm the presence of $O_2^{\bullet -}$ and $^1O_2$. In general, 5,5-dimethyl-pyridine-*N*-oxide (DMPO) and TEMPO as sensitive trapping agent to selectively capture $O_2^{\bullet -}$ and $^1O_2$. As shown in Figs. 4e and f, the EPR intensity of $O_2^{\bullet -}$ and $^1O_2$ in COF-NUST-36 were detected under light irradiation. When the illumination time is prolonged, the EPR intensities of $O_2^{\bullet -}$ and $^1O_2$ become stronger, which may be attributed to the accumulation of $O_2^{\bullet -}$ and $^1O_2$. However, no EPR signal is observed in the dark. Hence, $O_2^{\bullet -}$ and $^1O_2$ can be generated under light irradiation over COF-NUST-36.

Given the above experimental results and literature reports, a tentative reaction mechanism for the photocatalytic oxidation of benzylamine (BAN) over COF-NUST-36 was proposed (Fig. 5). This photocatalytic process is involved in both electron and energy

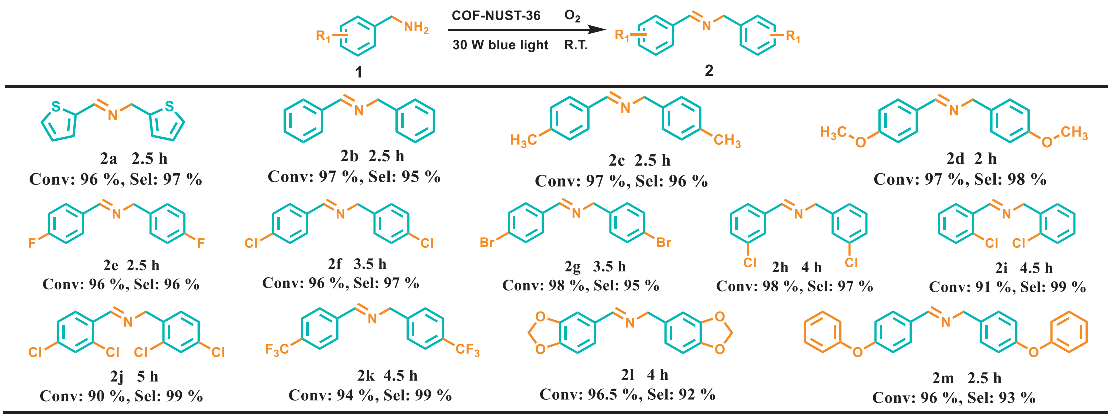

Scheme 1. Photocatalytic selective oxidative of diverse amines . Reaction conditions: substate (0.1 mmol), photocatalyst (4.0 mg), O_2 (1 atm), CH_3CN (1.5 mL), 30 W blue light (λ = 455–460 nm), room temperature. Determined by ^1H NMR. For details, see the Experimental section in Supporting information.

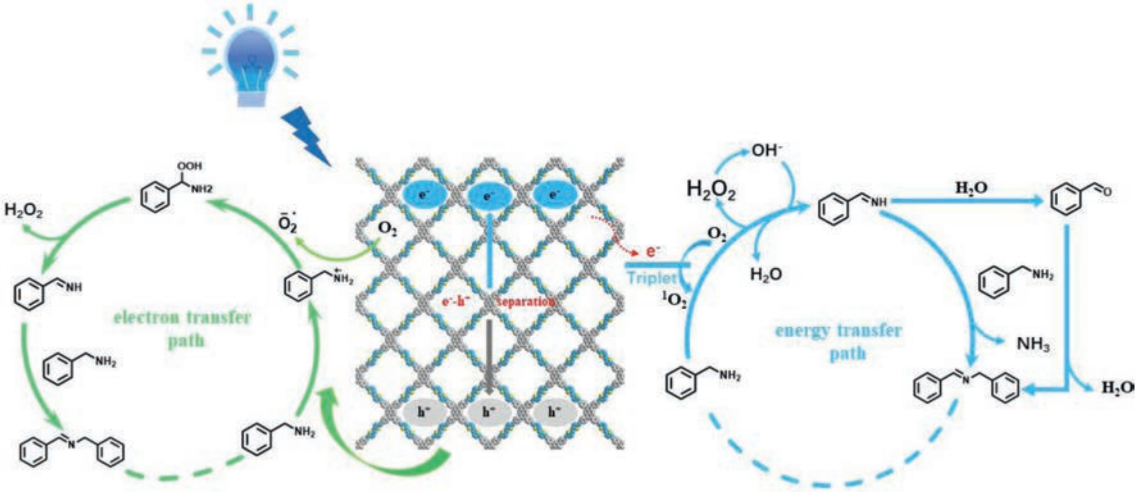

Fig. 5. Plausible mechanism for the photocatalytic selective oxidative coupling of benzylamine.

transfer path. The ground state COF-NUST-36 is photoexcited to the excited state COF-NUST-36* (electron–hole pairs) under blue light irradiation, the electron can reduce O_2 to generate $O_2^{\bullet -}$ in electron transfer path. At the same time, the BAN is oxidized to amine radical cation by COF-NUST-36^+. $O_2^{\bullet -}$ immediate react with amine radical cation to generate hydroperoxy(phenyl)methanamine. The hydroperoxy(phenyl)methanamine is extremely unstable, which can convert into PhCH=NH with the removal of H_2O_2. The intermediate PhCH=NH and H_2O_2 also can be obtained by extracting hydrogen atoms from the substrate directly through $^1O_2$ in an energy transfer path. The H_2O_2 can be dissociated into $^\bullet$OH under blue light irradiation, which is in favor for substrate to generate PhCH=NH. In the end, the PhCH=NH combine with BAN to obtain final product *N*-benzyl-1-phenylmethanimine. Furthermore, PhCH=NH is hydrolyzed to give benzaldehyde, which subsequently condensed with substrate to give the final product.

In summary, we proposed for the first time that the E_b of COF materials can be optimized by single atom substitution and extending conjugation strategy. A combination of temperature-dependent photoluminescence and electrochemical measurements reveals that the mesoporous COF-NUST-36 with less electronegativity of Se atoms and enhanced conjugation degree possesses the lowest E_b. The reduced E_b is helpful for the improvement of light capture and release of free charge carriers. Consequently, mesoporous COF-NUST-36 exhibited excellent photocatalytic performance for selective oxidation of amines under blue light. We believe that this work is not only benefit to understanding the relationship between exciton and photocatalytic activity at the atomic level, but also provides a new tactics for the design of advanced porous organic photocatalysts.

Declaration of competing interest

The authors have no conflict of interest.

Acknowledgments

This work was financially supported by the National Natural Science Foundation of China (No. 22171136), the Natural Science Foundation of Jiangsu Province (Nos. BK20220928, BK20220079), the Fundamental Research Funds for the Central Universities (Nos. 30921011102, 30922010902), the Medical Innovation and Development Project of Lanzhou University (No. lzuyxcx-2022-156), CAMS Innovation Fund for Medical Sciences (CIFMS, Nos. 2019-I2M-5-074, 2021-I2M-1-026, 2021-I2M-3-001), and the Startup Funding from Nanjing University of Science and Technology (Nos. AE89990, AE89991/376). G. Zhang acknowledges the support of the Thousand Young Talent Plan.

References

[1] S. Lin, C.S. Diercks, Y.B. Zhang, et al., Science 349 (2015) 1208–1213.
[2] C.J. Wu, X.Y. Li, T.R. Li, et al., J. Am. Chem. Soc. 144 (2022) 18750–18755.
[3] J. Zhou, J. Li, L. Kan, et al., Nat. Commun. 13 (2022) 4681.
[4] S. Li, L. Li, Y.J. Li, et al., ACS Catal. 10 (2020) 8717–8726.

[5] H. Chen, H.S. Jena, X. Feng, et al., Angew. Chem. Int. Ed. 61 (2022) e202204938.
[6] Y.N. Gong, X. Guan, H.L. Jiang, Coord. Chem. Rev. 475 (2023) 214889.
[7] C.X. Chen, Y.Y. Xiong, X. Zhong, et al., Angew. Chem. Int. Ed. 61 (2022) e202114071.
[8] A.P. Cote, A.I. Benin, N.W. Ockwig, et al., Science 310 (2005) 1166–1170.
[9] X.Y. Xu, P.Y. Cai, H.Z. Chen, et al., J. Am. Chem. Soc. 144 (2022) 18511–18517.
[10] R.Y. Liu, K.T. Tan, Y.F. Gong, et al., Chem. Soc. Rev. 50 (2021) 120–242.
[11] H.S. Lu, W.K. Han, X. Yan, et al., Angew. Chem. Int. Ed. 60 (2021) 17881–17886.
[12] X. Li, K. Zhang, G. Wang, et al., Nat. Synth. 1 (2022) 382–392.
[13] X. Wang, M. Bahri, Z.W. Fu, et al., J. Am. Chem. Soc. 143 (2021) 15011–15016.
[14] C. Yuan, S.G. Fu, K.W. Yang, et al., J. Am. Chem. Soc. 143 (2021) 369–381.
[15] X.Y. Wang, L.J. Chen, S.Y. Chong, et al., Nat. Chem. 10 (2018) 1180–1189.
[16] X. Ren, C. Li, W. Kang, et al., CCS Chem. 4 (2022) 2429–2439.
[17] X. Liu, X. Yang, X. Ding, et al., Chin. Chem. Lett. 34 (2023) 108148.
[18] L. Zou, R.J. Sa, H. Zhong, et al., ACS Catal. 12 (2022) 3550–3557.
[19] B. Han, X. Ding, B.Q. Yu, et al., J. Am. Chem. Soc. 143 (2021) 7104–7113.
[20] Y.L. Yang, H.Y. Niu, L. Xu, et al., Appl. Catal. B 269 (2020) 118799.
[21] D.W. Kang, J.H. Kim, J.H. Lim, et al., ACS Catal. 12 (2022) 9621–9628.
[22] D. Chen, W.B. Chen, G. Zhang, et al., ACS Catal. 12 (2022) 616–623.
[23] Q. Li, X.W. Lan, G.Y. An, et al., ACS Catal. 10 (2020) 6664–6675.
[24] A. Lopez-Magano, B. Ortin-Rubio, I. Imaz, et al., ACS Catal. 11 (2021) 12344–12354.
[25] H. Chen, W. Liu, A. Laemont, et al., Angew. Chem. Int. Ed. 60 (2021) 10820–10827.
[26] P. Shang, X. Yan, Y. Li, et al., Chin. Chem. Lett. 34 (2023) 107584.
[27] W.T. Wang, H.T. Wang, X.H. Tang, et al., Chem. Sci. 13 (2022) 8679–8685.
[28] H. Wang, S. Jin, X.D. Zhang, et al., Angew. Chem. Int. Ed. 59 (2020) 22828–22839.
[29] Adv. Energy. Mater. 10 (2020) 1903659.
[30] Y.Y. Qan, D.D. Li, Y.L. Han, et al., J. Am. Chem. Soc. 142 (2020) 20763–20771.
[31] H. Wang, W.X. Liu, X. He, et al., J. Am. Chem. Soc. 142 (2020) 14007–14022.
[32] N.C. Flanders, M.S. Kirschner, P. Kim, et al., J. Am. Chem. Soc. 142 (2020) 14957–14965.
[33] T. Banerjee, F. Podjaski, J. Kroger, et al., Nat. Rev. Mater. 6 (2021) 168–190.
[34] X. Zhang, K. Geng, G.D. Scholes, J. Am. Chem. Soc. 144 (2022) 16423–16432.
[35] Y. Liu, X. Jiang, L. Chen, et al., J. Mater. Chem. A 11 (2023) 1208–1215.
[36] H. Yu, D. Wang, JACS Au 2 (2022) 1848–1856.
[37] Z.A. Lan, G. Zhang, X. Chen, et al., Angew. Chem. Int. Ed. 58 (2019) 10236–10240.
[38] Q. Wang, X. Deng, H. Pen, et al., Nano Res. 16 (2023) 4225–4232.
[39] H. Lin, Y. Liu, Z. Wang, et al., Angew. Chem. Int. Ed. 61 (2022) e202214142.
[40] H. Chen, A. Wadsworth, C. Ma, et al., J. Am. Chem. Soc. 141 (2019) 18806–18813.
[41] G. Li, X. Zhang, L.O. Jones, et al., J. Am. Chem. Soc. 143 (2021) 6123–6139.
[42] Z. Zhang, Y. Li, G. Cai, et al., J. Am. Chem. Soc. 142 (2020) 18741–18745.
[43] Z.P. Li, Y.F. Zhi, P.P. Shao, et al., Appl. Catal. B 245 (2019) 334–342.
[44] Y. Su, B. Li, H. Xu, et al., J. Am. Chem. Soc. 144 (2022) 18218–18222.
[45] C.Z. Li, J.L. Liu, H. Li, et al., Nat. Commun. 13 (2022) 2357.
[46] X.D. Zhu, D.H. Li, R.J. Zhang, et al., Appl. Surf. Sci. 519 (2020) 146262.
[47] S. Tamariz, G. Callsen, J. Stachurski, et al., ACS Photonics 7 (2020) 1515–1522.
[48] M. Hamada, S. Rana, E. Jokar, et al., ACS Appl. Energ Mater. 3 (2020) 11830–11840.
[49] S. Duhovic, M. Dincă, Chem. Mater. 27 (2015) 5487–5490.
[50] G.L. Gibson, T.M. McCormick, D.S. Seferos, J. Am. Chem. Soc. 134 (2012) 539–547.
[51] W.L. Sheng, X.X. Wang, Y.X. Wang, et al., ACS Catal. 12 (2022) 11078–11088.
[52] H. Liu, C.Y. Xu, D.D. Li, et al., Angew. Chem. Int. Ed. 57 (2018) 5379–5383.
[53] Q. Li, J. Wang, Y.Z. Zhang, et al., ACS Appl. Mater Interfaces 13 (2021) 39291–39303.
[54] G. Li, P. Fu, Q. Yue, et al., Chem. Catal. 2 (2022) 1734–1747.
[55] Z.A. Lan, M. Wu, Z. Fang, et al., Angew. Chem. Int. Ed. 60 (2021) 16355–16359.
[56] W.J. Zhang, Z.Z. Deng, J.Y. Deng, et al., J. Mater. Chem. A 10 (2022) 22419–22427.
[57] S. Xue, W. Huang, W. Lin, et al., Chem. Catal. 2 (2022) 125–139.
[58] R. Chen, J.L. Shi, Y. Ma, et al., Angew. Chem. Int. Ed. 58 (2019) 6430–6434.
[59] J.L. Shi, R. Chen, H. Hao, et al., Angew. Chem. Int. Ed. 59 (2020) 9088–9093.